14th International Symposium on Turbulence and Shear Flow Phenomena (TSFP14)
Heidelberg, Germany, July 28–31, 2026

ON REYNOLDS NUMBER EFFECTS IN A SLENDER-BODY WAKE

Sanidhya Jain
Mechanical and Aerospace Engineering
University of California San Diego
CA 92093
saj004@ucsd.edu

Sutanu Sarkar
Mechanical and Aerospace Engineering
University of California San Diego
CA 92093
ssarkar@ucsd.edu

ABSTRACT

The flow past a canonical slender body without a trip is examined in a high-resolution numerical study where the length-based Reynolds number is systematically increased in the range, $Re = 9\times10^4$ to 6×10^5. The pre-separation boundary layer (BL) is no longer laminar at the higher values of the examined Re. The specific geometry is a 6:1 prolate spheroid. The focus of this case study is on how the Reynolds-number dependent flow separation affects the flow into the intermediate and far wake. Body forces, turbulence statistics and spectra are compared across the explored range of Re and, consequently, three regimes of flow evolution are determined based on BL separation.

INTRODUCTION

A slender-body geometry is widely used for aerial and underwater vehicles because of their superior drag characteristics. The size and operating speed, therefore, the Reynolds number, varies widely and depends on the application - from a mini AUV or mini UAS to the fuselage of a large aircraft. Systematic study of slender-body wakes started with Chevray (1968) who investigated the wake of a 6:1 prolate spheroid at $Re = 2.75\times10^6$. That work and more recent studies of axisymmetric slender bodies (Jiménez *et al.*, 2010; Posa & Balaras, 2016; Kumar & Mahesh, 2018; Ortiz-Tarin *et al.*, 2021) at Reynolds number of $O(10^5-10^6)$ have studied the flow into the near wake, $x/D < 20$. The first study (Ortiz-Tarin *et al.*, 2021) that probed slender-body evolution into the far wake was a wall-resolved LES whose domain reached $x/D = 80$ and had high resolution of the wake. That investigation at a length-based Reynolds number of $Re_L = 6\times10^5$ was performed with a trip to facilitate transition to turbulence in the boundary layer. Here, $Re = U_\infty L/\nu$ with L denoting the major-axis length, U_∞ the freestream velocity and ν the kinematic viscosity. . Contrary to axisymmetric bluff bodies, the typical vortex-shedding (VS) mode with azimuthal wave number of $m = \pm1$ that develops due to near-wake absolute instability was very weak for the 6:1 spheroid. $Re_D = U_\infty D/\nu$ based on the characteristic size normal to the flow is an alternate Reynolds number; for the 6:1 spheroid, $Re_D = Re/6$.

Given the uncertainties regarding the influence of the trip and trip-facilitated turbulence on the wake, we are motivated to examine a "cleaner" configuration where Reynolds number is the only controlling parameter. The twin foci of this parametric study of a canonical slender body - the 6:1 prolate spheroid - are the evolution of single-point statistics and the modal content of the unsteady fluctuations.

NUMERICAL METHODOLOGY

The numerical solver used for these simulations has been extensively validated in the past for body-inclusive simulations of wakes in homogeneous and density-stratified fluids (Ortiz-Tarin *et al.* (2019); Chongsiripinyo & Sarkar (2019)). The three-dimensional Navier-Stokes equations with the Boussinesq approximation (when considering a density-stratified fluid) in cylindrical coordinates is numerically solved. A third-order Runge-Kutta method combined with second-order Crank-Nicolson is employed to advance the equations in time. Second-order-accurate central differences are used for the spatial derivatives on a staggered grid. The dynamic Smagorinsky model is used to account for subgrid fluctuations. The boundary conditions are Dirichlet at the inflow, convective outflow and Neumann at the radial boundary. A synopsis of the flow solver in cylindrical coordinates, boundary conditions and immersed boundary method (IBM) approach is available in Chongsiripinyo & Sarkar (2019).

New simulations have been performed where the Reynolds number takes the following 4 values: $Re = 90,000$ in case R90, $Re = 180,000$ in R180, $Re = 300,000$ in R300 and $Re = 600,000$ in R600. Depending on the value of Re, the cases exhibit boundary layers that range from laminar to turbulent. R600, which is the most computationally demanding case, is simulated with a $748\times512\times7168$ grid (about 2.8 billion grid points) that spans a cylindrical computational domain that extends up to $x = 48D$ and has diameter $10D$.

The boundary layer is well resolved with about 21 points across it in case R90 and 70 in case 600. To assess grid quality, the ratio of grid spacing to the Kolmogorov length, denoted as $\eta = (\nu^3/\varepsilon)^{1/4}$, is computed in all three directions. In the R90 wake, the ratios of streamwise (Δx), radial (Δr), and azimuthal

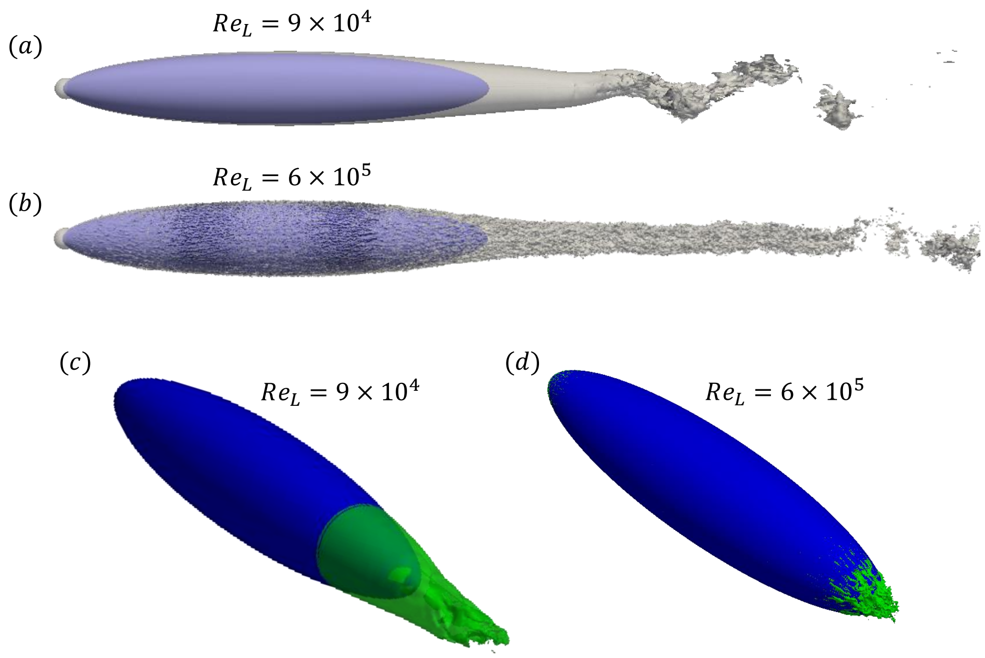

Figure 1. Comparison of R90 ($Re = 9 \times 10^4$ with R600 ($Re = 6 \times 10^5$) using instantaneous flow visualization. Panels (a) and (b) show the isocontour of the streamwise velocity, $u_x = 0.75U_\infty$. Panels (c) and (d) visualize the boundary of the separation bubble with the $u_x = 0$ contour.

($r\Delta\theta$) grid spacing to η stay below 8, 1 and 6, respectively. For the highest Re case R600, the ratio of Δx, Δr, and $r\Delta\theta$ to η stay below 11, 5 and 2, respectively. Thus, the current LES are at high resolution.

RESULTS

After achieving statistical stationarity, all statistics have been computed over a time-resolved ensemble of at least $170tU_\infty/D$ (convective time units), with the low-Re cases having an ensemble time span as large as $300tU_\infty/D$. The length of the time series is found to be good enough for sufficiently resolving the most energetic motions. For example, the ensemble for R90 wake with the energetically dominant vortex shedding frequency of $St \approx 0.36$ spans about 100 complete cycles.

Figure 1 illustrates the qualitative difference between R90 and R600 using instantaneous flow visualizations. R90 exhibits laminar boundary layer separation whereas R600 does not. The recirculation region in R600 is much smaller than in case R90. Interestingly, the near wake (Fig. 1 (a)) at the lower Re of R90 shows signs of a sinuous mode and the energy spectrum (as will be discussed) peaks at a frequency of $St = fD/U_\infty \approx 0.36$.

Boundary layer transition and body forces

Surface shear gives insights into the BL and its separation. Figure 2 shows the normal gradient of the surface velocity (du_s/dn) for R180, R300 and R600. For $Re = 1.8 \times 10^5$, high shear can be observed at the nose, gradually decreasing over the length of the body. This is a characteristic laminar boundary layer. When Re is increased to 3×10^5, streaky patches of high shear start advecting along the surface with the flow. The boundary layer has begun a transition from laminar, but has not become fully turbulent. Finally, at the highest Re of 6×10^5, the boundary layer has transitioned to turbulence with small scale structures appearing in the surface shear field. Furthermore, unlike the lower-Re cases, there is an elongated patch of elevated shear near the central region of the spheroid. This has previously been observed for similar slender body objects with a tripped boundary layer (Kumar & Mahesh, 2018; Posa & Balaras, 2016).

Figure 3 presents the spatial distribution of the time-averaged Reynolds shear stress, $\overline{u_r'u_x'}$, near the body for three different Reynolds numbers. At the lowest $Re = 1.8 \times 10^5$, $\overline{u_r'u_x'} \approx 0$ over the body, indicative of a laminar BL. Negative $\overline{u_r'u_x'}$ appear only after the laminar separation at $x/D \approx 4$, coinciding with the flow becoming turbulent, as shown later using TKE evolution (figure 5b). As Re is increased to 3×10^5, negative $\overline{u_r'u_x'}$ can be observed on the body in the boundary layer for $x/D > 0$, a region comprising of an adverse pressure gradient (APG) due to geometry. In R300, there is a gradual increase of $\overline{u_r'u_x'}$ from negligible values at $x/D = 0$ to negative in the aft portion of spheroid, indicating a transitional boundary layer before eventual separation. At the highest Re case of 6×10^5, the onset of the negative shear stress shifts significantly upstream, indicating that the boundary layer has transitioned from laminar flow much earlier and remains transitional/turbulent over the majority of the body. Interestingly, the presence of favorable pressure gradient (FPG) for $x/D < 0$ does not force the BL to be laminar for this sufficiently large $Re = 6 \times 10^5$.

The drag coefficient (C_d), defined as $C_d = F_d/(0.5\rho U_\infty^2 A)$ where $A = \pi D^2/4$ and F_d is the drag force, and its partition into pressure and skin friction (shear) components is shown in figure 4. Skin friction is the dominant contributor to C_d for all Re cases. Consistent with a laminar boundary layer for the R90 and R180 cases, multiplying $C_f(x)$ by $(Re)^{1/2}$ collapses the streamwise evolution of local skin-friction coefficient between these two cases (figure not shown). Pressure contribu-

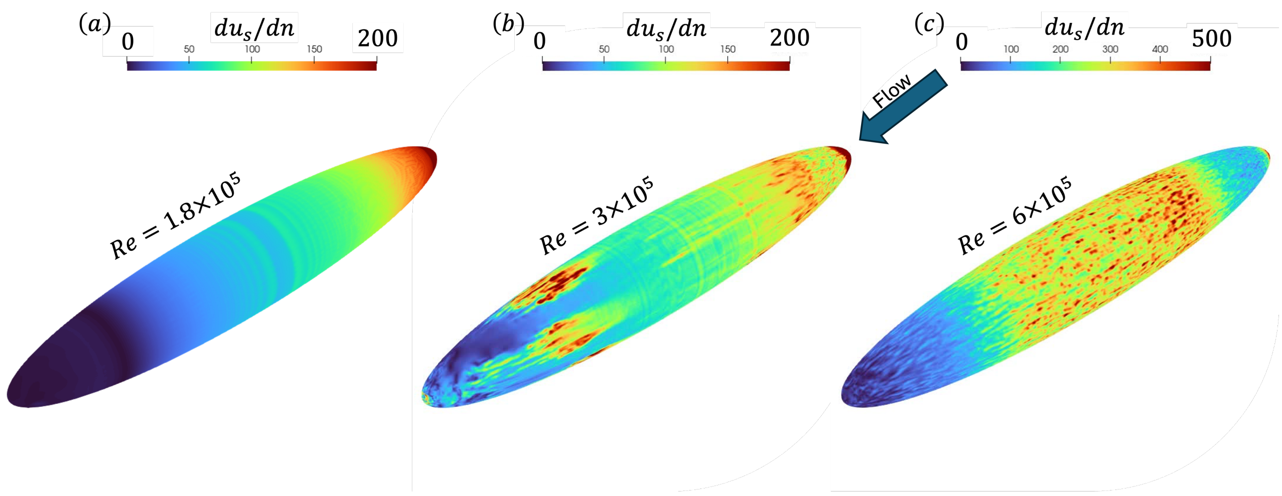

Figure 2. Normal gradient of surface velocity du_s/dn: (a) R180, (b) R300 and (c) R600. Increasing the Re leads to transition of the boundary layer from laminar to turbulent.

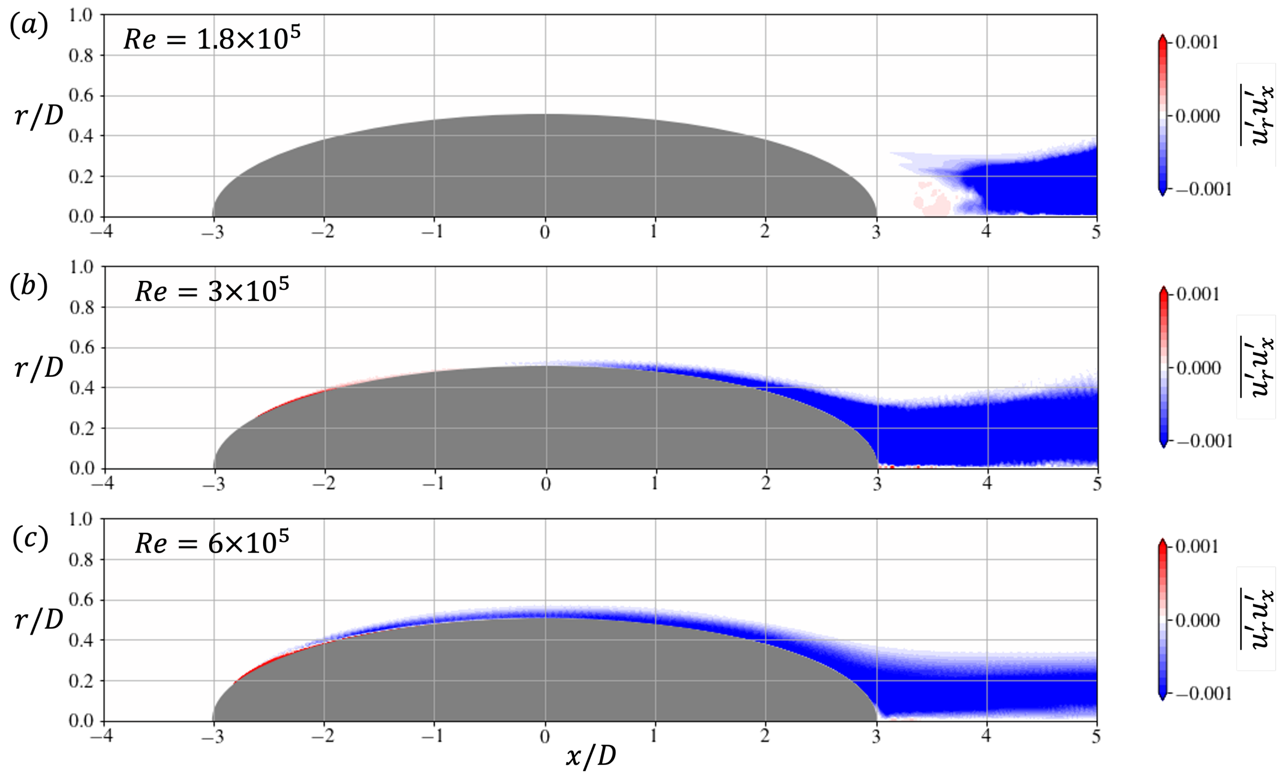

Figure 3. Contours of Reynolds stress $\overline{u'_r u'_x}$ for (a) R180, (b) R300 and (c) R600.

tion remains mostly unchanged for $Re < 3\times10^5$, whereas it reduces by approximately a factor of 4 as Re is increased to 6×10^5. Furthermore, since the body is aligned with the flow, i.e., unpitched, the transverse force components (C_y and C_z) are negligible compared to the drag for all Re, not shown for brevity.

Wake evolution

The streamwise evolution of peak defect velocity is shown for each case in figure 5(a). For R90 and R180, there is an initial plateau up to $x/D \approx 4.5$ corresponding to a laminar separation bubble. The plateau is followed by a rapid monotonic decay after $x/D \approx 4.5$, the onset of turbulent wake entrainment. For R300, the decay starts immediately after leaving the body at $x/D = 3$ and, after $x/D = 7$, the wake evolves as $U_d^{peak} \sim x^{-1.16}$. The R600 boundary layer is turbulent and it relatively late separation creates the smallest separation bubble (figure 1d). Since, the R600 wake is the narrowest among all cases with the least initial entrainment, it also exhibits the slowest initial decay of U_d^{peak}. The value of $U_d^{peak}(x)$ is consistently higher in R600 - approximately a factor of 3.5 - relative to the other cases. R600 exhibits $U_d^{peak} \sim x^{-4/3}$ after $x/D = 10$, i.e., a slightly higher decay than the R300 case.

We move on to turbulence quantification with figure 5(b) that shows the area-integrated turbulent kinetic energy ($\{E_K^T\}$) where the integral is over $x =$ constant cross-sections. For R90 and R180, during the transition from laminar separation to turbulence, there is a rapid increase of $\{E_K^T\}$ until $x/D \approx 5.5$.

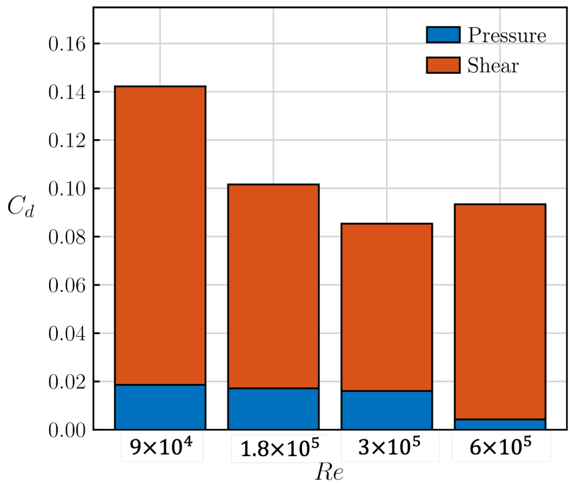

Figure 4. Drag coefficient (C_d) along with its pressure and shear components for R90, R180, R300 and R600.

Beyond $x/D \approx 5.5$, both low-Re cases decay with the same rate, $\{E_K^T\} \sim x^{-1}$. For the higher Re case of R300, the transition to turbulence has significantly moved upstream and occurs on or very close to the body. Thus, the turbulent kinetic energy shows a monotonic decay for the entire wake domain and, furthermore, $\{E_K^T\} \sim x^{-2/3}$, exhibits a decay rate that is shallower than the x^{-1} exponent of the low-Re cases. The evolution of $\{E_K^T\}$ is qualitatively different. Unlike all the other cases, R600 does not show any significant decay for the entire domain. Also, the peak $\{E_K^T\}$ is much lower than all the other Re cases.

In order to clarify the case-dependent TKE evolution , we take a closer look at the components of the TKE transport equation, specifically, the production (P) and dissipation (ε). Figure 6 shows the streamwise evolution of the ratio of area-integrated production and dissipation ($\{P\}/\{\varepsilon\}$). It reveals three distinct regimes:

I - For low-Re ($Re = 9\times10^4$ and 1.8×10^5 (not shown)), $\{P\}/\{\varepsilon\} > 1$ initially, injecting energy into the TKE budget. It drops below 1 after $x/D = 5.5$ and, correspondingly, TKE decays.
II - For $Re = 3\times10^5$, $\{P\}/\{\varepsilon\} < 1$ for the entire wake and TKE exhibits a monotonic decay.
III - At the highest $Re = 6\times10^5$, an extended region of $\{P\}/\{\varepsilon\} > 1$ is observed up to $x/D = 20$. Beyond this point, $\{P\}/\{\varepsilon\}$ drops below 1 and TKE commences its decay.

To summarize, the I, II and III regimes classified based on $\{P\}/\{\varepsilon\}$ point to a qualitative effect of BL transition, its separation and the immediate near wake on the subsequent behavior of the wake up to $x/D = 45$.

Spectral analysis

The flow past the spheroid - an axisymmetric body - is nominally axisymmetric and is also statistically steady. Thus, the time-resolved velocity fluctuations ($\mathbf{u}'(r,\theta,x,t)$) can be scale-decomposed into $\hat{\mathbf{u}}'(r,m,x,St)$) by performing 2D DFT in the azimuthal and temporal directions. For the azimuthal mode $m \in [-N_\theta/2,\ldots,N_\theta/2-1]$ and the temporal frequency bin $k \in [0,\ldots,N_t-1]$, the normalized forward 2D DFT is given as

$$\hat{\mathbf{u}}'(r,m,x,f_k) = \frac{1}{N_\theta N_t}\sum_{n=0}^{N_t-1}\sum_{j=0}^{N_\theta-1}\mathbf{u}'_{j,n}(r,x)e^{-i2\pi\left(\frac{jm}{N_\theta}+\frac{kn}{N_t}\right)}$$

The discrete physical frequency for bin k is $f_k = \frac{k}{N_t\Delta t}$. This is converted to the non-dimensional Strouhal number using the characteristic length D and free-stream velocity U_∞ as $St_k = f_k D/U_\infty$.

The spectral TKE density (ϕ_K) for a specific discrete mode and frequency bin is calculated from the inner product of the resulting complex Fourier coefficients:

$$\phi_K(r,m,x,St_k) = \frac{1}{2}\langle\hat{\mathbf{u}}(r,m,x,St_k)\cdot\hat{\mathbf{u}}^*(r,m,x,St_k)\rangle$$

For a radial grid consisting of discrete points r_i for $i = 0,1,\ldots,N_r-1$ and the area of the annular cell $A_i \approx 2\pi r_i \Delta r_i$, the area-integrated spectral TKE at each x-location is given as

$$\int E_K^T\, dA \approx \sum_{i=0}^{N_r-1}\phi_K(r_i,m,x,St_k)A_i$$

Figure 7 shows spectra of area-integrated spectral TKE density on log scale ($\log_{10}(\int E_K^T\, dA)$ as a function of (m,St) for $Re = 1.8\times10^5$ for three streamwise locations $x/D = 3, 10$ and 40. At the trailing edge of the body ($x/D = 3$), only the ($m = 0, St = 0$) mode, which is quasi-steady and axisymmetric, is evident. This location is inside the separation bubble and the wake has not yet become turbulent. Downstream at $x/D = 10$, after the wake has becomes unstable, the helical vortex-shedding mode ($m = \pm1$) at $St \approx \pm0.4$ is energetically dominant. There is significant energy at $m = \pm2$ and $St = 0, \pm0.4, \pm0.8$ too, hinting at a significant non-linear energy transfer due to triadic interactions of the vortex shedding mode with itself. Towards the end of the computational domain at $x/D = 40$, the vortex shedding mode is still significant implying a long lifetime of these modes.

It is noted that the energy content for the positive and negative m modes at the same St are different. This is due to the directional preference of the helical modes, where $m = +1$ is an anticlockwise helix and -1 is clockwise. Since, $m = +1$ has more energy compared to $m = -1$, the dominant orientation of the helical mode appears to be anticlockwise. More analysis is required to determine the reason for this preference and the mechanism for switching between these two modes. Also, there is a reflectional symmetry in the spectra where $(+m,+St)$ is equivalent to $(-m,-St)$ by definition.

Figure 8 shows that the spectra for $Re = 6\times10^5$ (R600) are significantly different than their lower-Re counterparts. Even at $x/D = 3$ (trailing edge), the fluctuation energy is distributed across a wide range of scales and frequencies (broadband spectrum), emphasizing the contrast with the laminar separation for R90. Nevertheless, the quasi-steady ($m = \pm1, St = 0$) mode is the most energetic here. Further downstream at $x/D = 10$ and $x/D = 40$, it is found that the $m = \pm1$ azimuthal mode remains dominant throughout the domain but it is no longer quasi-steady. The $m = \pm1$ mode for R600 exhibits a peak frequency - the vortex-shedding frequency - at $St \approx 0.25$, although it is not a discrete peak as for R90; here, the energy is spread across multiple frequencies. For R600, although asymmetry still exists between $+m$ and $-m$ modes, the level of asymmetry is much smaller compared to R180.

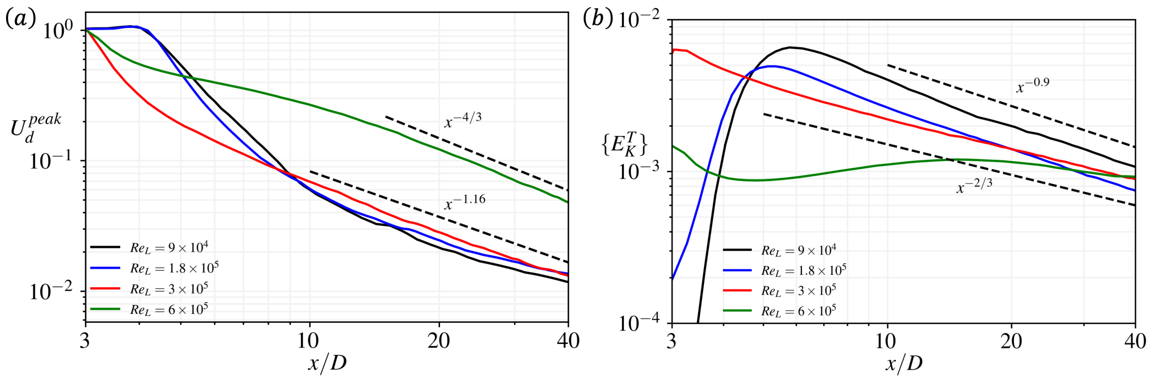

Figure 5. Comparison of wake statistics between R90, R180, R300 and R600: (a) Peak defect velocity (U_d), (b) Area-integrated TKE ($\{\phi_K\}$).

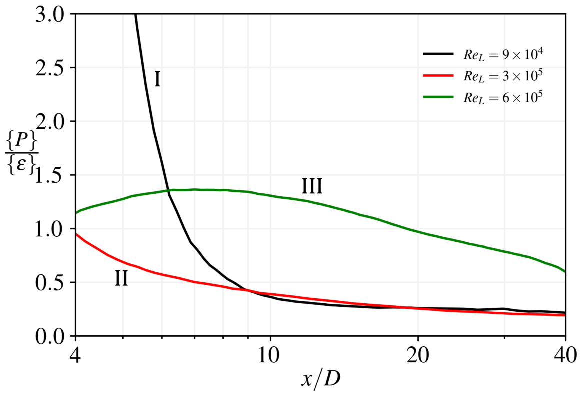

Figure 6. Ratio of area-integrated production and dissipation ($\{P\}/\{\varepsilon\}$). $\{P\}/\{\varepsilon\} < 1$ indicate dissipation being higher than production, leading to a decay in TKE. Labels I, II and III correspond to different *Re*-regimes of wake-turbulence evolution.

Contours of TKE at different streamwise locations $x/D = 3, 10$ and 40 are shown in figure 9(a) for R180. Initially axisymmetric at $x/D = 3$, the TKE contour elongates preferentially along one direction at $x/D = 10$ and stays like that throughout the domain. This is likely due to preferential orientation of the vortex shedding plane. Orientation of this plane, however, can change with time, sometimes with a very low frequency (VLF) (Rigas *et al.*, 2014). Since, these VLF frequencies can be approximately two orders of magnitude less than the shedding frequency, resolving them requires a much longer time series, beyond the scope of this study.

At separation ($x/D = 3$), the R600 wake is much narrower compared to R180 (figure 9b) due to the turbulent BL being more resistant to separation. This leads to a significantly smaller wake throughout the domain compared to R180. Furthermore, the wake remains axisymmetric for the entire domain.

ACKNOWLEDGEMENTS

We gratefully acknowledge the support of the Office of Naval Research grant N0014-20-1-2253.

REFERENCES

Chevray, R. 1968 The turbulent wake of a body of revolution. *J. Basic Eng* **90**, 275–284.

Chongsiripinyo, K. & Sarkar, S. 2019 Decay of turbulent wakes behind a disk in homogeneous and stratified fluids. *J. Fluid Mech.* **885**, A31.

Jiménez, J. M., Hultmark, M. & Smits, A. J. 2010 The intermediate wake of a body of revolution at high Reynolds numbers. *J. Fluid Mech.* **659**, 516–539.

Kumar, P. & Mahesh, K. 2018 Large-eddy simulation of flow over an axisymmetric body of revolution. *J. Fluid Mech.* **853**, 537–563.

Ortiz-Tarin, J.L., Nidhan, S. & Sarkar, S. 2021 High-reynolds-number wake of a slender body. *J. Fluid Mech.* **918**.

Ortiz-Tarin, J. L., Chongsiripinyo, K. C. & Sarkar, S. 2019 Stratified flow past a prolate spheroid. *Phys. Rev. Fluids* **4** (9), 094803.

Posa, A. & Balaras, E. 2016 A numerical investigation of the wake of an axisymmetric body with appendages. *J. Fluid Mech.* **792**, 470–498.

Rigas, G., Oxlade, A. R., Morgans, A.S. & Morrison, J. F. 2014 Low-dimensional dynamics of a turbulent axisymmetric wake. *J. Fluid Mech.* **755**, R5.

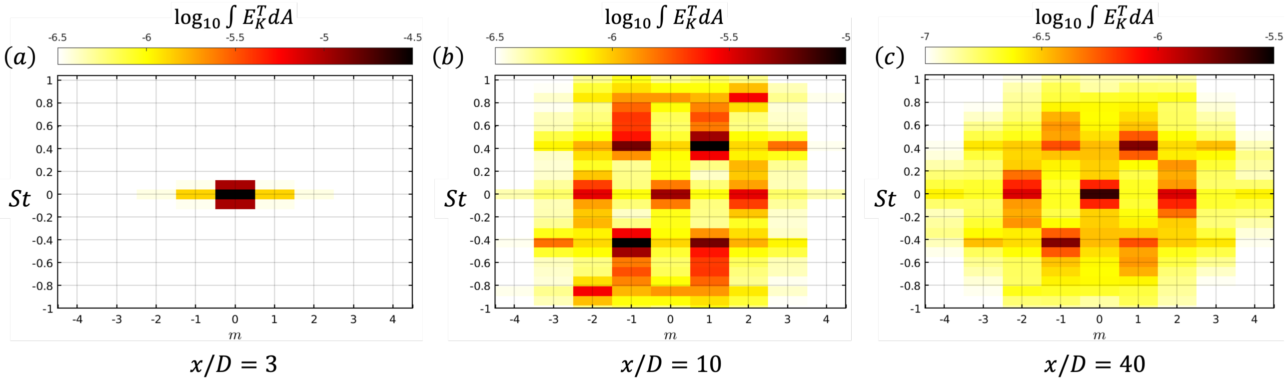

Figure 7. Azimuthal and temporal spectra for area-integrated TKE (log-scale) of $Re = 1.8 \times 10^5$ at (a) $x/D = 3$, (b) $x/D = 10$ and (a) $x/D = 40$. Here, horizontal axis is the azimuthal mode number m and vertical axis is the non-dimensional temporal frequency St.

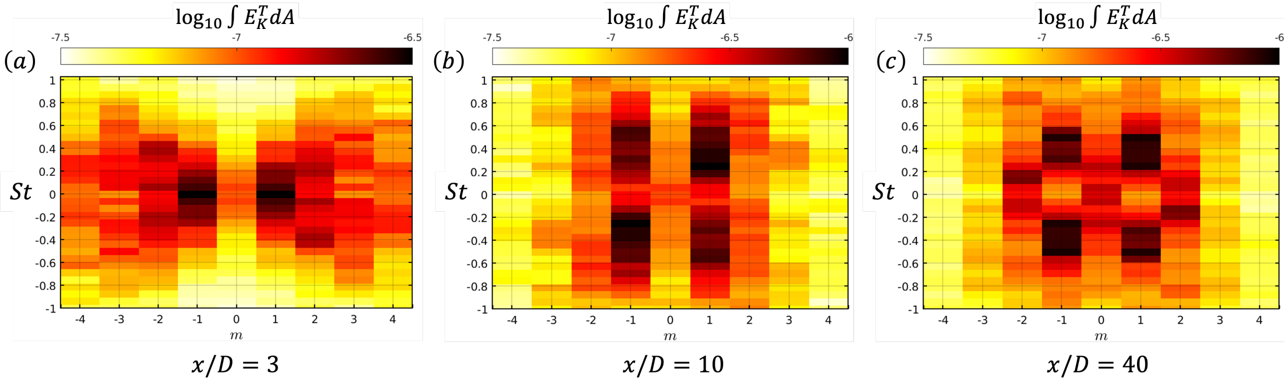

Figure 8. Same as figure 7 for $Re = 6 \times 10^5$.

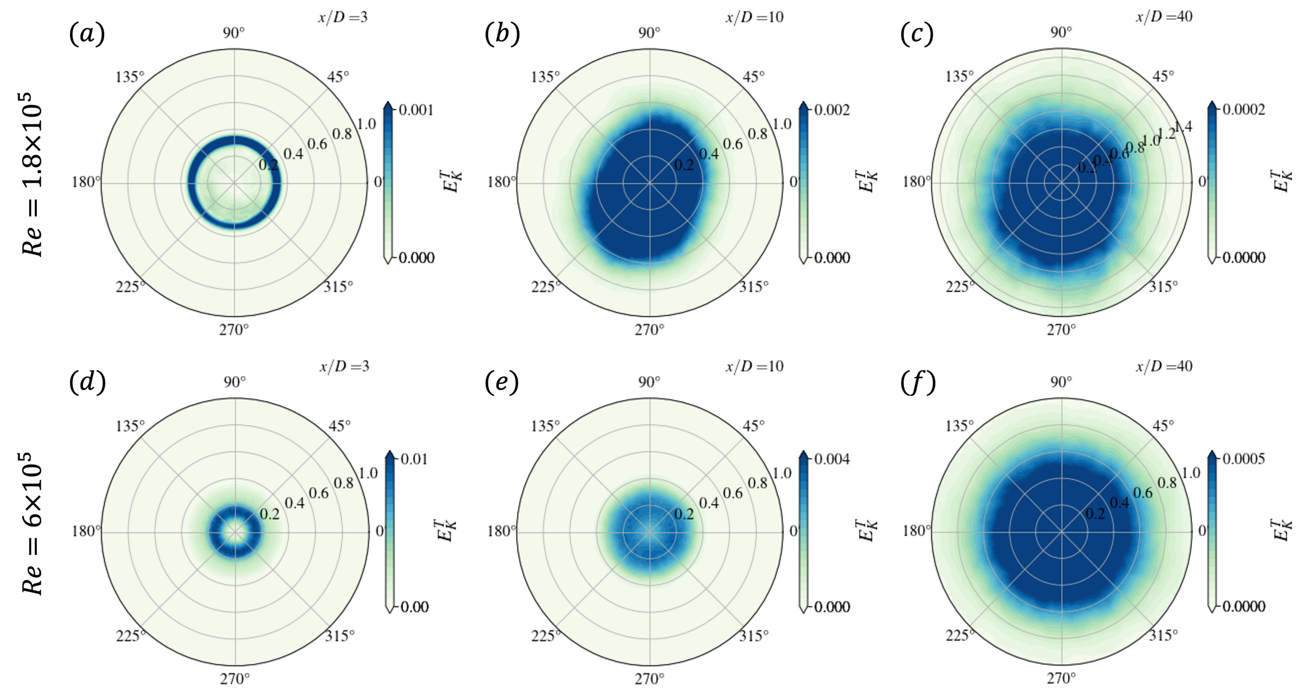

Figure 9. TKE (ϕ_K) contours for streamwise locations $x/D = 3, 10$ and 40: (a-c) R180 and (d-f) R600.